Chemical Engineering Journal 519 (2025) 165419

Contents lists available at ScienceDirect

Chemical Engineering Journal

journal homepage: www.elsevier.com/locate/cej

Efficient aqueous activation of boron nitride colloidal catalysts for enhanced selective methane oxidation under mild conditions

Younhwa Kim [a], Hobin Kwak [a], Chanhee Choi [a], Hyesung Choi [a], Sungsu Kang [a], Chan Kim [a,f], Yongmin Kim [f], Jungwon Park [a,b,c,d,e,*]

[a] School of Chemical and Biological Engineering, Institute of Chemical Processes, Seoul National University, Seoul 08826, Republic of Korea
[b] Center for Nanocrystal Research, Institute for Basic Science (IBS), Seoul 08826, Republic of Korea
[c] Institute of Engineering Research, College of Engineering, Seoul National University, Seoul 08826, Republic of Korea
[d] Advanced Institute of Convergence Technology, Seoul National University, Suwon 16229, Republic of Korea
[e] Hyundai Motor Group-Seoul National University (HMG-SNU) Joint Battery Research Center (JBRC), Seoul National University, Seoul 08826, Republic of Korea
[f] Center for Hydrogen and Fuel Cell Research, Korea Institute of Science and Technology (KIST), Seoul 02792, Republic of Korea

ARTICLE INFO

Keywords:
Boron nitride
Activation
Boron oxide
Selective methane oxidation
C1 oxygenates

ABSTRACT

Non-metal hexagonal boron nitride (BN) catalysts hold significant promise for the selective oxidation of light alkanes due to their distinctive anti-overoxidation properties. Although reaction-induced BO_x species are typically considered the active phase, their formation within the inert BN lattice often requires harsh activation conditions and high reaction temperatures, limiting the production of value-added liquid oxygenates at low temperatures. In this study, we demonstrate that active BO_x species can be efficiently generated on boron nitride colloids (BNC) through a simple hydrothermal treatment at 140 °C in a clean aqueous environment. A combination of spectroscopic and microscopic investigations reveals that these BO_x species develop at lattice-disordered boron sites along the edges of BN particles. Mechanistic studies, supported by theoretical calculations, indicate that BO_x formation follows radical-driven pathways, facilitated by the simultaneous activation of H_2O and O_2 on disordered boron species. By utilizing the activated BNC catalysts for low-temperature selective methane oxidation below 80 °C with H_2O_2 as a green oxidant, we achieved approximately four times higher C1 oxygenate productivity (31.7 mmol g_{cat}^{-1} h^{-1}) compared to non-activated BNC, while maintaining high selectivity (>90%) and good reusability over 10 cycles.

1. Introduction

Hexagonal boron nitride (BN), composed of alternating boron and nitrogen atoms in a honeycomb-like structure, is an emerging non-metal catalyst noted for its environmentally benign elements, high chemical stability, and resistance to overoxidation in the oxidative conversion of important alkanes. [1–3] Recently, its applications have expanded to include the selective oxidation of methane—one of the most challenging reactions in catalysis [4–8]—into value-added chemicals [9]. Methane, the primary component of abundant natural gas, possesses the strongest C—H bond among hydrocarbons (440 kJ mol^{-1}) and negligible electron affinity, often resulting in overoxidation into CO or CO_2 byproducts in oxidative environments [10–13]. To address this challenge, numerous metal-based catalysts have been explored for the selective conversion of methane into liquid oxygenates [14–18]. Notably, BN catalysts exhibit high performance with very low CO_2 selectivity, outperforming conventional metal catalysts, which are typically used in bulk powder form without significant structural modifications [9]. However, unrefined BN powder often requires high reaction temperatures (>500 °C) to overcome its chemical inertness and activate the exceptionally strong C—H bond in methane, particularly when using molecular O_2 as the oxidant. Such harsh reaction conditions inevitably lead to significant energy consumption and low selectivity (~33%) for value-added liquid oxygenates due to excessive CO formation.

Previously, we demonstrated that defect-engineered boron nitride colloids (BNC) exhibit notable mass activity and over 90% selectivity for the selective oxidation of methane to C1 oxygenates (CH_3OOH, $HOCH_2OOH$, CH_3OH, and HCOOH) at mild temperatures (~100 °C)

* Corresponding author at: School of Chemical and Biological Engineering, Institute of Chemical Processes, Seoul National University, Seoul 08826, Republic of Korea.
E-mail address: jungwonpark@snu.ac.kr (J. Park).

https://doi.org/10.1016/j.cej.2025.165419
Received 7 March 2025; Received in revised form 6 June 2025; Accepted 26 June 2025
Available online 3 July 2025

using H_2O_2 as a green oxidant, outperforming both fresh BN powder and conventional metal catalysts [19]. This remarkable performance arises from reaction-induced BO_x species, generated on lattice-disordered boron sites in N-vacancies of BNC, which facilitate H_2O_2 activation and significantly increase the production of important radical intermediates (e.g. •CH_3, •OH, •OOH) due to enhanced structural flexibility. However, the working temperatures for BNC (~100 °C) remain higher than those of conventional metal catalysts such as Rh [20], AuPd [21]-based catalysts, and Cu- or Fe-exchanged zeolites [22,23], which can operate efficiently even below 80 °C. This is because activating BN to form reactive BO_x species typically requires high temperatures due to its inherent chemical inertness, leading to elevated reaction temperatures for the selective oxidation of methane and other light alkanes [24]. Therefore, developing efficient pre-activation methods to form active BO_x species on BN using oxidants is essential for achieving selective methane oxidation under milder conditions.

To date, various top-down strategies, including plasma treatment [25,26], chemical functionalization with H_2SO_4 or NaOH [27,28], and high-temperature steam activation (>850 °C) [29], have been explored to functionalize hexagonal BN, avoiding the complex steps inherent in bottom-up synthesis [1]. However, these methods often require restricted solvents or extreme temperatures. More importantly, a robust and efficient approach to generating active BO_x species for direct methane oxidation has yet to be demonstrated. This highlights the need for simple, environmentally friendly activation methods capable of producing active BO_x species under mild conditions for selective methane oxidation at significantly lower temperatures.

In this study, we developed a low-temperature hydrothermal method that effectively activates BNC catalysts in a clean aqueous environment by facilitating the formation of active BO_x species. Spectroscopic and microscopic analyses revealed that these BO_x species form on lattice-disordered boron sites near the edges of BNC. Mechanistic studies, including theoretical calculations, showed that active BO_x species are generated through radical-driven mechanisms involving the activation of both H_2O and O_2. When using the activated BNC catalysts for selective methane oxidation below 80 °C with H_2O_2 as a green oxidant, the catalyst mediated the formation of •CH_3, •OOH, and •OH radicals, leading to approximately 4 times higher C1 oxygenate productivity (31.7 mmol g_{cat}^{-1} h^{-1}) than non-activated BNC, with high selectivity (>90%) and no significant loss of activity over 10 cycles. Beyond its immediate application to methane valorization under mild conditions, this work offers a broader framework for tuning the surface chemistry of boron nitride materials. Given their versatility across a range of fields—as quantum emitters [30], substrates [31], catalyst supports [11,32–34], and nonmetal catalysts [19]—our approach provides simple and environmentally friendly methods for tailoring their properties.

2. Methods

2.1. Preparation of BN and BNC samples

Fresh BN powder was prepared by calcining commercial hexagonal BN (Alfa Aesar, 99.5%) at 500 °C (ramp rate 5 °C min^{-1}) for 5 h under airflow. The BNC catalyst was obtained as described in the reference [19]. Specifically, 2 g of air-calcined BN powder was treated in 200 mL of 3 M HCl at 90 °C overnight and subsequently washed with deionized water until reaching neutral pH. After that, 0.05 g of HCl-treated BN was dispersed in 50 mL of deionized water and exfoliated by sonication at 500 W for 1 h. The colloidal particles were then collected by centrifugation at 3000 rpm for 10 min, repeated twice.

For H_2O/air- or H_2O_2/air-activated BNC samples, 40 mL of BNC solution, without or with 1.6 mL of H_2O_2 (SAMCHUN, 30%), was transferred to a Teflon-coated stainless-steel autoclave. Hydrothermal treatment was conducted at target temperatures for 5 h. Activated BNC samples were collected by evaporating the solvent in an oven at 80 °C for 2–3 days, followed by re-dispersion in deionized water through sonication for 1 h, maintaining the original concentration.

For the H_2O/Ar activation, the BNC solution was transferred into a batch reactor system connected to Ar gas. The compactly sealed reactor was purged with Ar five times to eliminate residual air, then heated and maintained at 140 °C for 5 h. For air activation, BNC was dried as a powder by evaporating the water solvent in the oven at 80 °C for 2–3 days, then transferred to the autoclave and heated at 140 °C for 5 h. The air-activated BNC was subsequently exfoliated in deionized water by sonication for 1 h.

2.2. Characterizations

The Fourier transform infrared (FT-IR) spectra were obtained using a Vertex-80 V/Hyperion2000 (Bruker). The X-ray photoelectron spectroscopy (XPS) analysis was performed using a Versaprobe III from RIAM. The XPS spectra were calibrated by adjusting the binding energy of the C 1 s peak to 284.5 eV. Solid-state electron paramagnetic resonance (EPR) was performed using Bruker EMXmicro-9.8/2.7 spectrometer with an X-band frequency of 9.46 GHz. The near-edge X-ray absorption fine structure (NEXAFS) spectra at the B K-and N K-edge were measured at the 4D beamline of the Pohang Accelerator Laboratory using both total electron yield (TEY) and partial electron yield (PEY) detection modes. X-ray diffraction (XRD) analysis was performed using a Rigaku diffractometer (Cu Kα radiation, 40 kV, 30 mA). Raman spectroscopy was performed using a confocal microscope (NOST-HEDA) equipped with an Ar laser operating at 532 nm. The scanning electron microscopy (SEM) images were obtained using a Hitachi SU8230. The transmission electron microscopy (TEM) images were obtained using a JEM-2100F (JEOL) microscope operating at 200 kV. The high-angle annular dark-field scanning TEM (HAADF-STEM) images and electron energy loss spectroscopy (EELS) mapping were acquired using a JEOL JEM-ARM200F with a probe corrector and Gatan GIF Quantum ER spectrometer at the National Center for Inter-university Research Facilities (NCIRF), Seoul National University. To capture radicals during H_2O/air activation, H_2O_2/air activation, and the reaction, 5,5-dimethyl-1-pyrroline N-oxide (DMPO, Sigma-Aldrich, 97%) was used as a spin-trapping agent. After activation or reaction at the target temperatures for the specified duration, the mixture was cooled to below 10 °C. A 1 mL liquid product sample was quickly mixed with 0.5 mL of DMPO (20 mg mL^{-1} in methanol) and subsequently analyzed by EPR. In situ diffuse reflectance infrared Fourier transform spectroscopy (in situ DRIFTS) data for H_2O/air activation process were collected using a Thermo Scientific Nicolet 8700 FTIR spectrometer. A heated HATR-IR (horizontal attenuated total reflection infrared) flow-through cell equipped with a ZnSe crystal was used to monitor new functional groups in the BNC catalyst after exposure to an H_2O/air flow (30 mL min^{-1}) for 10 min at 140 °C. Water was introduced via air passing through a water bubbler. For in situ DRIFTS under methane oxidation environment, the samples were heated to 80 °C, and 0.2 M H_2O_2 was introduced by passing methane (10 mL min^{-1}) through a bubbler. The sample holder was initially filled with fresh BN to eliminate empty space, followed by placing the solid H_2O/air-BNC(140) catalyst on the surface. The specimens for XPS, NEXAFS, XRD, Raman, and SEM measurements were prepared by drop-casting the sample solution onto a silicon wafer and subsequently drying it at 70 °C overnight. The samples for FT-IR, solid-state EPR, and in situ DRIFTS spectroscopy were prepared in a powder form by evaporating the solvent from BN colloids at 70 °C for 2–3 days.

2.3. Selective methane oxidation

The process of selective methane oxidation was conducted within a Teflon-coated stainless-steel autoclave reactor containing a 120 mL quartz vessel. Generally, 40 mL of 200 mM H_2O_2 aqueous solution containing 20 mL of colloidal catalysts was introduced into the vessel. After sealing the autoclave, the reactor underwent five cycles of flushing with 95% CH_4/N_2 and was pressurized to 30 bar. The mixture was

heated to the desired temperatures and agitated at 1000 rpm for 30 min. After the reaction, the reactor was rapidly cooled in an ice bath to below 10 °C to prevent product volatilization.

Liquid-phase products were analyzed by ^{1}H NMR spectroscopy (600 MHz, Bruker) employing solvent-suppression techniques after filtration for catalyst removal. 0.7 mL of liquid sample was mixed with 0.1 mL D_2O containing 3-(trimethylsilyl)-1-propanesulfonic acid sodium salt (DSS). The total organic carbon content in the liquid sample was quantified using a Total Organic Carbon Analyzer (SHIMADZU). Gas-phase products were analyzed via online gas chromatography (GC-6500 series; Younglin) using Molsieve 13× and Porapak N columns. Signal detection was carried out using a thermal conductivity detector (TCD) for N_2, and CH_4, and a flame-ionization detector (FID) equipped with a methanizer for CO, and CO_2. Gaseous products were measured repeatedly under reduced pressure to minimize potential interference from CO_2 dissolution. The amount of H_2O_2 consumed using potassium titanium(IV) oxalate spectrophotometry and UV–vis detection. The gain factor is defined as the molar ratio of produced C1 oxygenates to consumed H_2O_2.

The reusability test was conducted by collecting the catalyst after the initial cycle. It was evaporated in an 80 °C oven for 2–3 days and then exfoliated in fresh deionized water via sonication for 1 h, maintaining the same concentration as in the first reaction.

The productivity and selectivity of the products were determined using the following formulas:

$$\text{Productivity}\left(\text{mmol}\, g_{cat}{}^{-1}\, \text{h}^{-1}\right) = \frac{mol\,(specific\ product)}{weight\ of\ catalyst\,(g) \times reaction\ time\,(h)}$$

$$\text{Selectivity}\ (\%) = \frac{mol\ (C1\ oxygenates)}{mol\ (CH_3OOH) + mol\ (HOCH_2OOH) + mol\ (CH_3OH) + mol\ (HCOOH) + mol\ (CO_2)} \times 100\%$$

The apparent activation energy (E_{app}) was calculated by analyzing the Arrhenius plot, which involves plotting ln(CH_4 conversion rate) against 1/T over a range of temperatures. The methane conversion rates were determined using the following formula:

$$CH_4\ \text{conversion rate}\left(\text{mmol}\, g_{cat}{}^{-1}\, \text{h}^{-1}\right) = \frac{mol\ (CH_3OOH) + mol\ (HOCH_2OOH) + mol\ (CH_3OH) + mol\ (HCOOH) + mol\ (CO_2)}{weight\ of\ catalyst\ (g) \times reaction\ time\ (h)}$$

2.4. Density functional theory (DFT) calculations

All DFT calculations were performed using the Vienna Ab initio Simulation Package (VASP), version 6.2.0, employing the generalized gradient approximation (GGA) with the Perdew-Burke-Ernzerhof (PBE) exchange-correlation functional [35]. The interactions between core and valence electrons were modeled using the projector-augmented wave (PAW) method. For geometric optimizations, a plane-wave energy cutoff of 520 eV was used, with Brillouin zone sampling conducted on a 3 × 3 × 1 Monkhorst-Pack k-point grid. Van der Waals interactions were included through Grimme's DFT-D3 method.

A three-layer hexagonal BN (002) slab with a 20 Å vacuum was constructed, allowing relaxation for the top two layers while keeping the bottom layer fixed. The $BN_{0.94}$ model, featuring disordered boron species interconnected between layers, was generated by removing two nitrogen atoms from the top layer and one from an adjacent layer [19]. The $BN_{0.98}$ model, with a point nitrogen vacancy and preserved crystalline layered structure, was created by removing one nitrogen atom from the top layer of the pristine BN model. Geometry optimization convergence criteria were set at 1×10^{-5} eV for energy and 0.03 eV Å^{-1} for force.

For H_2O/air activation transition states, the climbing-image nudged elastic band (CI-NEB) method was applied. A lower energy cutoff of 400 eV and a 1 × 1 × 1 k-point mesh were used for Brillouin zone sampling, with convergence criteria of 1×10^{-5} eV and 0.06 eV Å^{-1} for energy and force.

3. Results and discussion

3.1. Direct methane oxidation using activated BNC catalysts

The fresh BNC catalyst was prepared by washing commercial hexagonal BN powder with HCl, followed by 1 h of sonication and centrifugation to remove larger particles and collect the colloid (details provided in the Supporting Information). The HCl treatment generated nitrogen point vacancies, while subsequent sonication positioned these vacancies in adjacent layers, inducing the formation of lattice-disordered boron species (Figs. S1 and S2). After that, the fresh BNC catalyst was activated via hydrothermal treatment in either deionized water or a 0.2 M H_2O_2 solution under air exposure at various temperatures (denoted as H_2O/air-BNC(activation temperature, ^{o}C) and H_2O_2/air-BNC(activation temperature, ^{o}C), respectively). The activated BNC catalysts were then tested for low-temperature selective methane oxidation in the liquid phase at 80 °C using H_2O_2 as a green oxidant (Fig. 1a and Table S1). Without methane, no carbon products were produced after the reaction (Fig. S3). Compared to commercial B_2O_3 and fresh BN powder, which showed low C1 oxygenates productivities of 5.3 and 2.6 mmol g_{cat}^{-1} h^{-1}, respectively, the fresh BNC catalyst exhibited higher productivity (7.6 mmol g_{cat}^{-1} h^{-1}) due to its lattice-disordered defects [19].

Notably, H_2O/air activation significantly enhanced C1 oxygenates productivity, reaching 31.7 mmol g_{cat}^{-1} h^{-1} at an optimal hydrothermal temperature of 140 °C. This value is approximately four times higher than that of the fresh BNC catalyst, highlighting its potential as a promising non-metal alternative with competitive performance (Tables S2 and S3). The total organic carbon measured in the solvent was consistent with the quantified product yield (Fig. S4). At extended reaction times and elevated temperatures, HCOOH was newly formed, suggesting it is an over-oxidized product (Figs. S5 and S6). In addition, the use of O_2 as a co-oxidant slightly enhanced C1 oxygenate productivity and increased the selectivity toward more oxidized and stable products, such as $HOCH_2OOH$ and HCOOH, at the same H_2O_2 concentration (Fig. S7). As the C1 oxygenates primarily consist of CH_3OOH and $HOCH_2OOH$, they can be easily collected as important CH_3OH via

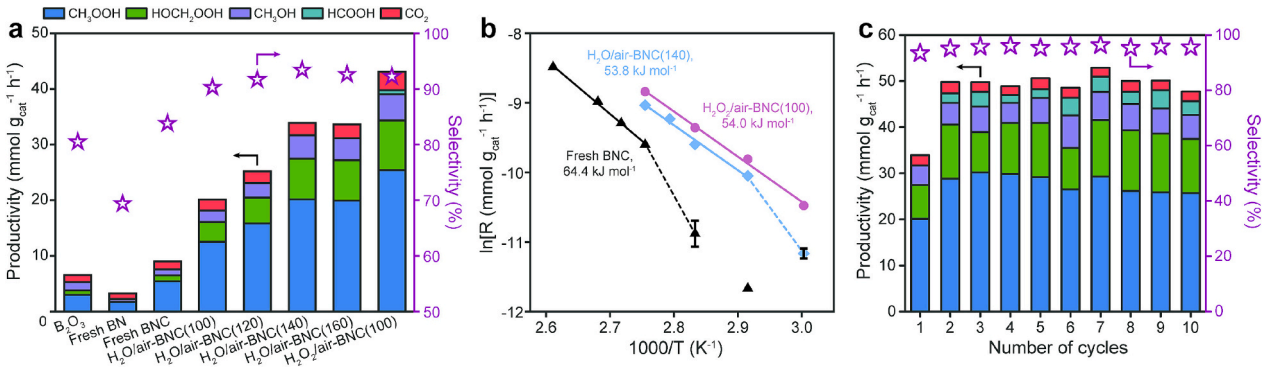

Fig. 1. (a) Catalytic performance of commercial B_2O_3, fresh BN, fresh BNC, and BNC catalysts activated in H_2O/air or H_2O_2/air at different temperatures. The round brackets indicate the activation temperatures. Reaction conditions: 30 bar of 95% CH_4/N_2, 80 °C, 0.5 h, 0.2 M of H_2O_2, 40 mL of liquid, 2 mg of catalysts, 1000 rpm. (b) Arrhenius plots for fresh BNC, H_2O/air-BNC(140), and H_2O_2/air-BNC(100). R represents CH_4 consumption rates. The error bars show standard deviations from three independent tests. (c) Reusability test for H_2O/air-BNC(140) at 80 °C.

simple $NaBH_4$ reduction [19]. Additionally, H_2O_2/air activation was also found to effectively activate the BNC catalyst, achieving optimal performance at 100 °C (Fig. S8). This lower optimal hydrothermal temperature, compared to the 140 °C required for H_2O/air activation, reflects the stronger oxidation capability of H_2O_2. However, raising the activation temperature to 120 °C significantly decreases C1 oxygenate production, likely due to excessive oxidation and degradation of BO_x species in BNC (Fig. S9).

Arrhenius plots were obtained to estimate apparent activation energies and evaluate the impact of activation on BNC catalyst productivity at various reaction temperatures (Fig. 1b). For non-activated BNC, a significant increase in productivity was observed around 90 °C, suggesting that new phases—possibly active BO_x species, where oxygen is incorporated into lattice-disordered boron species of multiple N-vacancies [19]—may form at higher temperatures, leading to elevated optimal reaction temperatures. Notably, the transition point shifted to approximately 70 °C for H_2O/air-BNC(140), while H_2O_2/air-BNC(100) showed no transition point. In addition, compared to the non-activated BNC, which had an activation energy of 64 kJ mol^{-1}, H_2O/air-BNC(140) and H_2O_2/air-BNC(100) showed reduced apparent activation energies of 54 kJ mol^{-1}, highlighting the importance of activation in lowering optimal reaction temperatures. In recyclability tests, H_2O/air-BNC(140) demonstrated good stability, showing no significant decrease in activity or selectivity after 10 cycles (Fig. 1c). The increased productivity observed after the first cycle is likely attributed to additional activation occurring during the reaction at 80 °C, where H_2O_2 functions as an oxidant. In contrast, non-activated BNC consistently exhibited low productivity after the first cycle (Fig. S10).

The gain factor was 0.11 for H_2O/air-BNC(140), significantly higher than that of fresh BNC (0.01), highlighting the importance of H_2O/air activation in enhancing H_2O_2 utilization efficiency (Fig. S11). In non-activated BNC, uncoordinated boron at nitrogen vacancies can promote undesirable H_2O_2 dissociation, lowering oxidant efficiency [36]. In contrast, H_2O/air activation and additional activation during reaction facilitate the catalytically active species at nitrogen vacancies, suppressing non-productive H_2O_2 decomposition. The increased gain factor of 0.18 after 1 h of reaction and 0.15 after multiple reaction cycles further confirms the improved efficiency achieved through activation. Therefore, pre-activation of BNC is essential for enhancing both C1 oxygenate production and H_2O_2 utilization efficiency at lower reaction temperatures, and even environmentally benign aqueous conditions can effectively activate BNC catalysts.

3.2. Formation of BO_x species in BNC after activation

The enhanced catalytic activity observed in H_2O/air activation prompted an investigation into structural changes in BNC catalysts. We

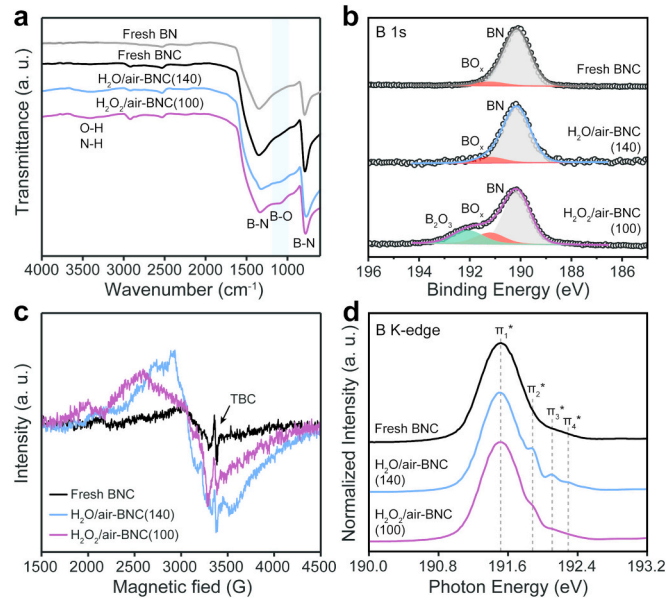

Fig. 2. (a) FT-IR spectra of fresh BN, fresh BNC, H_2O/air-BNC(140), and H_2O_2/air-BNC(100). (b) XPS, (c) EPR, and (d) B K-edge NEXAFS spectra of fresh BNC, H_2O/air-BNC(140), and H_2O_2/air-BNC(100). The TBC in EPR spectra indicates three boron centers. The NEXAFS spectra are normalized by adjusting the intensity of the 1 s → π* absorption peak to 1.

focused on H_2O/air-BNC(140) and H_2O_2/air-BNC(100), which demonstrated the highest activity in selective methane oxidation. X-ray diffraction analysis confirmed that the overall hexagonal structures of the BNC catalysts remained intact after activation (Fig. S12). Raman spectroscopy revealed a 1 cm^{-1} upshift in the E_{2g} band of BNC catalysts compared to fresh BN, indicating fewer lateral layers than bulk BN powder (Fig. S13) [37].

The FT-IR spectra of fresh BN and BNC catalysts exhibited characteristic in-plane B—N stretching (~1340 cm^{-1}) and out-of-plane bending (~780 cm^{-1}) vibrations (Fig. 2a) [27]. In BNC catalysts, the intensity around 3404 cm^{-1}, attributed to O—H species at BN edges [38], increased due to the removal of less hydrophilic particles after water sonication and centrifugation. Following H_2O/air activation, a peak at ~1075 cm^{-1}, corresponding to B—O species from either BO_x or B_2O_3 species, emerged alongside an intensified O—H peak, indicating the structural transformation of BNC during hydrothermal treatment. The FT-IR spectrum of H_2O_2/air-BNC(100) showed a stronger B—O peak and a comparable O—H peak intensity relative to H_2O/air-BNC(140).

Given that H_2O_2/air-BNC(100) demonstrated higher C1 oxygenate productivity than H_2O/air-BNC(140), B—O species from either BO_x or B_2O_3 appear more closely associated with the active phase than B–OH species at BN edges. XPS analysis further confirmed an increase in moderately oxidized BO_x species after H_2O/air activation, while over-oxidized B_2O_3 species were detected only after H_2O_2/air activation (Fig. 2b) [39,40]. The proportions of BO_x species among total boron species in fresh BNC, H_2O/air-BNC(140), and H_2O_2/air-BNC(100) were 2.8%, 7.2%, and 8.8%, respectively (Table S4). After the first reaction cycle of H_2O/air-BNC(140), the BO_x content increased from 7.2% to 11.7%, corresponding to the enhanced C1 oxygenate productivity observed after the initial cycle. It also suggests that there is additional in situ activation during the reaction at 80 °C, where H_2O_2 acts as an oxidant (Fig. S14 and Table S4). With extended reaction cycles, the proportion of B_2O_3 species are gradually increased, whereas the BO_x content remained constant, indicating that these BO_x species are structurally stable under repeated reaction conditions. Commercial B_2O_3 powder exhibited inferior C1 oxygenates productivity, as shown in Fig. 1a. Additionally, the increasing B_2O_3 content showed little correlation with productivity, suggesting that B_2O_3 or boron species originating from B_2O_3 dissolution, which may form through repeated sonication that tears BN sheets and exposes new edge sites susceptible to oxidation by H_2O_2 [41], play a minimal role in C1 oxygenate production (Fig. S15). In contrast, a clear linear correlation was identified between the proportion of BO_x species and C1 oxygenate productivity, supporting that the stable BO_x species functions as catalytically active sites in selective methane oxidation. The N 1 s XPS spectra revealed no significant changes in nitrogen species throughout the reaction cycles (Fig. S16).

The significantly higher activity of fresh BNC compared to fresh BN powder in selective methane oxidation is primarily attributed to the presence of disordered boron species within multiple N-vacancies [19]. The EPR spectra of fresh BNC revealed asymmetric and broad resonance peaks over a wide range (3000 G), attributed to disordered boron species (Fig. 2c) [42]. A sharp peak at 3360 G (g = 2.0044) corresponds to nitrogen point vacancies, where three ^{11}B atoms are positioned at equal distances [43]. Following H_2O/air or H_2O_2/air activation, the broad EPR peak intensity increased, indicating a higher concentration of unpaired electrons trapped in the BN lattice, while the signal for nitrogen point vacancies showed minimal change (Fig. S17). As shown in Fig. 2a and b, the FT-IR and XPS analyses confirmed that the activation led to the formation of BO_x species, suggesting that the increase in unpaired electrons after H_2O/air or H_2O_2/air activation is attributed to the incorporation of hetero oxygen atoms into disordered boron species [44,45].

The insertion of oxygen atoms into disordered boron species and the formation of BO_x species in BNC catalysts after activation were further confirmed by NEXAFS analysis (Fig. 2d). The B K-edge spectra showed an absorption peak around 191.5 eV (π_1*), corresponding to the 1 s ➔ π* transition in BN_3 species [46,47], and the spectra were normalized to this π_1* transition. Notably, activated BNC catalysts exhibited additional peaks at 191.9 eV (π_2*), 192.1 eV (π_3*), and 192.3 eV (π_4*), indicating B 1 s → π* transitions in oxygen-incorporated BN_2O and BNO_2 species [48–50]. This confirms the embedding of oxygen atoms into the BN lattice at original N positions, forming BO_x species. In contrast, no significant changes were observed at nitrogen sites after activation (Fig. S18). Furthermore, after the five reaction cycles, BO_x species in BNC remained detectable, confirming their structural stability (Fig. S19).

3.3. Microscopic investigation of BNC after H_2O/air activation

The SEM image of H_2O/air-BNC(140), acquired in secondary electron mode, shows uniform sheet-like particles (~1 μm) compared to bulk BN powders (Figs. 3a and S20). The red laser beam is clearly visible through the BNC solution, indicating well-dispersed colloids in DI water (inset of Figs. 3a and S21). The TEM image of a representative H_2O/air-BNC(140) catalyst particle shows a morphology similar to that of non-activated BNC (Figs. 3b and S22). The sheet-like morphology and stacking layers of H_2O/air-BNC(140) were retained after multiple reaction cycles (Figs. S23 and S24). To ascertain the location of oxygen-incorporated BO_x species, side-view observation was conducted using HAADF-STEM on a focused-ion-beam processed specimen with carbon protection layers. The HAADF-STEM images, along with EELS analysis, reveal that oxygen species are primarily present at the surface near the edge sites rather than in the center of the BNC sheets (Figs. 3c, S25, and S26). In addition, the extracted EELS spectra of B, N, and O species from the STEM image also indicate that B—O species from BO_x are predominantly observed in the surface region. In addition, the top-view HAADF-STEM images also reveal disordered regions in the H_2O/air-BNC(140) and the incorporated oxygen atoms into nitrogen vacancies (Fig. S27).

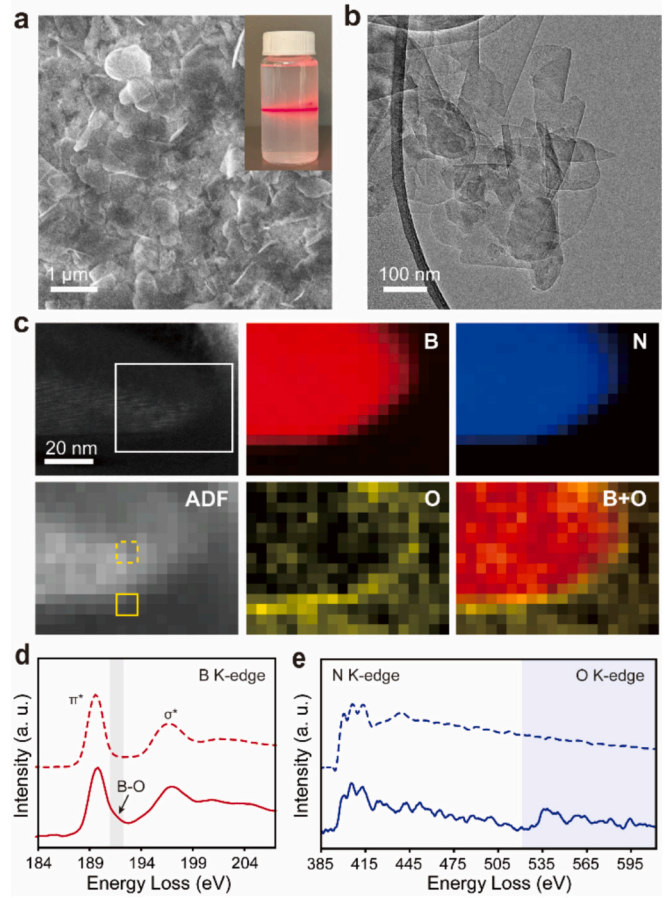

Fig. 3. (a) Secondary electron and digital image of H_2O/air-BNC(140) showing Tyndall effect, (b) TEM images of H_2O/air-BNC(140), (c) Cross-sectional HAADF-STEM image of H_2O/air-BNC(140), along with the ADF (annular dark field) image and EELS mapping results within the white box, (d, e) EELS spectra of the boron, nitrogen, and oxygen K-edges for the yellow solid and dotted boxes in (c).

3.4. Investigation of the activation mechanism of BNC catalysts in aqueous environment

Compared to the H_2O/air environment, BNC catalysts activated in an H_2O/argon environment or in an air environment without H_2O exhibit lower C1 oxygenate productivity (Fig. 4a). This indicates that both H_2O and O_2 molecules are involved in forming BO_x species throughout BNC catalyst activation. Additionally, mass spectrometric analysis of gaseous products during activation confirms that H_2O activation excludes a hydrogen production-mediated mechanism (Fig. S28) [51]. The intermediates formed during H_2O/air activation of the BNC catalyst were

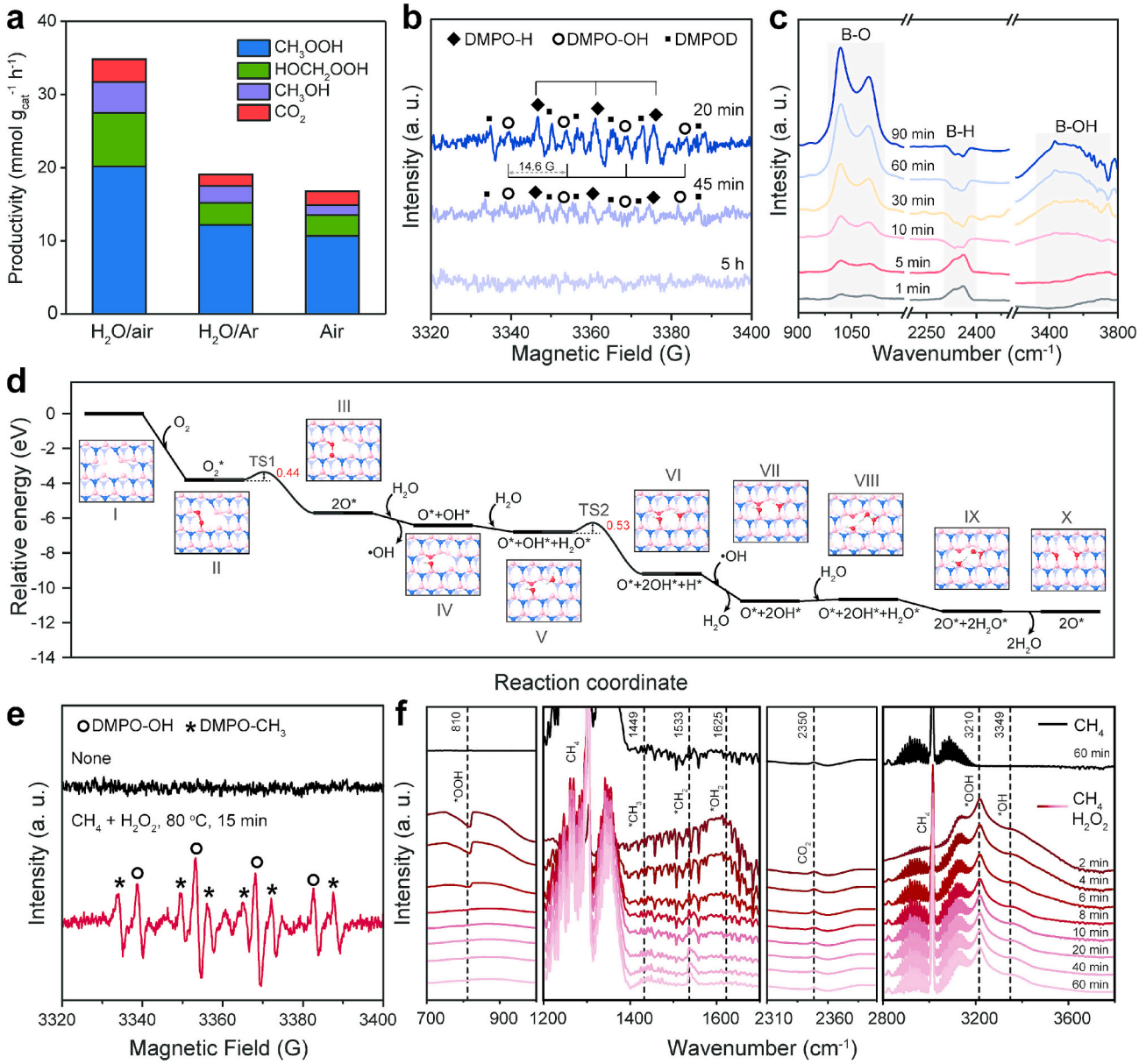

Fig. 4. (a) Catalytic performance of BNC catalysts after activation under H_2O/air, H_2O/Ar, and air environments at 140 °C for 5 h. Reaction conditions: 30 bar of 95% CH_4/N_2, 80 °C, 0.5 h, 0.2 M of H_2O_2, 40 mL of liquid, 2 mg of catalysts, 1000 rpm. (b) EPR spectra of DMPO-captured radicals after H_2O/air activation of BNC at 140 °C for 20 min, 45 min, and 5 h. DMPOD represents the degradation radical of DMPO, a carbon-centered radical formed through oxidation of DMPO. (c) in situ DRIFT spectra obtained during the activation of BNC under H_2O/air flow at 140 °C. (d) DFT-calculated free energy diagram for the H_2O/air activation process on the $BN_{0.94}$ model. (e) EPR spectra of DMPO-captured radicals after methane oxidation over H_2O/air-BNC(140). Reaction conditions: 30 bar of 95% CH_4/N_2, 80 °C, 15 min, 0.2 M of H_2O_2, 40 mL of liquid, 2 mg of catalysts, 1000 rpm. (f) In situ DRIFTS measurement following exposure to CH_4 alone or $CH_4 + H_2O_2$ at 80 °C over H_2O/air-BNC(140).

then investigated using DMPO as a radical scavenger. After 20 min of H_2O/air activation, DMPO-H and DMPO-OH species were detected by EPR spectroscopy, confirming a radical-driven pathway (Fig. 4b). The intensity of these •H and •OH radicals gradually decreased and eventually disappeared, suggesting their consumption in the formation of BO_x species. In the case of H_2O_2/air activation at 100 °C, an excess amount of DMPO-OH was generated (Fig. S29).

The formation of BO_x species in BNC during H_2O/air activation was further investigated using in situ DRIFTS. Fig. 4c illustrates the spectral changes observed after exposing fresh BNC to H_2O/air for 10 min at 140 °C. Notably, a peak at ~3700 cm^{-1}, assigned to B–OH species anchored on oxidized boron species [52], and a peak at ~2350 cm^{-1}, corresponding to B—H species [53], appeared early in the activation process and gradually diminished as peaks at 960–1150 cm^{-1} attributed to BO_x species [50], significantly increased. The negative value of B—H peak arises because DRIFTS measurements were taken after 10 min of H_2O/air activation, during which some B—H species had already formed. These findings suggest that B–OH anchored on oxidized boron and B—H species can be formed during H_2O/air activation at low temperatures (~140 °C) and serve as precursors to BO_x species, whereas the activation of conventional BN powder by H_2O or O_2 typically requires temperatures above 500 °C due to the inertness of the BN structure [24]. Additionally, the peak at ~3480 cm^{-1}, attributed to B–OH species at BN edges–less relevant for C1 oxygenates production–intensified in the later activation stages.

We further explored the molecular mechanism of the H_2O/air activation process on BNC catalysts using DFT calculations (Fig. 4d). As shown in Figs. 2c and S17, EPR results revealed that disordered boron

species play a more crucial role in BO_x formation than nitrogen point vacancies, which contain crystalline boron species at equal distances. Our previous studies indicate that disordered boron species form when N-vacancy sites are positioned near each other in adjacent interlayers [19]. Therefore, we employed a $BN_{0.94}$ model with two N-vacancies in the topmost layer and one in the second layer, as this configuration induces significant structural deformation and the formation of disordered boron species (Fig. S30, Step I in Fig. 4d).

It has been theoretically predicted that O_2 chemisorption at one of the B—B sites near multiple N-vacancies in the $BN_{0.94}$ model is thermodynamically favorable, leading to the formation of peroxo-like BO–OB species without an energy barrier (II, Fig. S31) [24]. The O—O bond then cleaves with an energy barrier of 0.44 eV (TS1), generating terminal B—O and oxygen-incorporated B–O–B species (III). This terminal B—O species stabilizes into B–OH through H_2O dissociation, producing •OH radicals (IV), as also confirmed by EPR and in situ DRIFTS results (Fig. 4b and c). Subsequently, another H_2O molecule is introduced (V) and dissociates at a different B—B site, forming B—H and B–OH species (VI) with an energy barrier of 0.53 eV (TS2). The •OH radical, generated from H_2O dissociation on terminal B—O species, abstracts H atoms from B—H species, which are then extracted by an H_2O molecule (VII). This mechanism aligns with the observed decrease in B—H intensity in the in situ DRIFT spectra (Fig. 4c). In the presence of H_2O, a water molecule bridges between the remaining two B–OH species via hydrogen bonding, thereby enabling proton transfer (VIII and IX) [24]. The newly formed H_2O then desorbs from the surface, leading to the formation of oxygen-incorporated BO_x species (X). This indicates that both O_2 and H_2O function as oxidants in the generation of active BO_x species, while H_2O also serves as a proton donor throughout the activation process. An alternative •OOH radical-mediated pathway for H_2O/air activation is predicted to be less favorable (Fig. S32). Additionally, the $BN_{0.98}$ model, which contains nitrogen point vacancies in the first layer to mimic crystalline boron species at regular distances, exhibits a higher energy barrier of 0.73 eV in the O_2 dissociation step (Fig. S33). This suggests that disordered boron species in $BN_{0.94}$ model enable more facile activation of H_2O or O_2 compared to crystalline boron species, consistent with EPR results showing that nitrogen point vacancies remain unchanged after activation (Fig. S17).

We further performed DMPO-EPR analysis to investigate the reaction intermediates involved in selective methane oxidation over H_2O/air-BNC(140) at 80 °C (Fig. 4e). After reaction at 80 °C for 15 min, distinct peaks corresponding to DMPO-CH_3 and DMPO-OH were observed. In situ DRIFT analysis further revealed that co-feeding CH_4 and H_2O_2 at 80 °C, compared to CH_4 feeding alone, led to a substantial increase in *OOH (810 and 3210 cm^{-1}) and *OH (3349 cm^{-1}) species during the initial stage of the reaction (Fig. 4f), followed by an increase in *CH_3 (1449 cm^{-1}) and *CH_2 (1533 cm^{-1}) species, with only low levels of CO_2 (2350 cm^{-1}) observed [54–56]. These results indicate methane oxidation over H_2O/air-BNC(140) proceeds via a radical-mediated mechanism involving the formation of •CH_3, •OOH, and •OH intermediates, initiated by H_2O_2 dissociation. Additionally, DFT calculations show that the energy barrier for CH_4 or H_2O_2 dissociation, producing highly reactive terminal B—O species [19], is lower than that required for BO_x formation on disordered boron sites via H_2O/air activation (Figs. S34). This suggests that pre-formation of BO_x sites is crucial, as they serve as active centers for C1 oxygenate production but cannot readily form at low temperatures. The H_2O/air pre-activation step facilitates BO_x site formation by overcoming this energy barrier, thereby significantly enhancing C1 oxygenate productivity at lower temperatures compared to non-activated BNC catalysts (Fig. S35).

4. Conclusions

In conclusion, BNC catalysts can be effectively activated to form reactive BO_x species in an aqueous environment at low temperatures (~140 °C), eliminating the need for harsh functionalization conditions typically required for the selective oxidation of light alkanes. The H_2O/air activation enhances C1 oxygenate productivity (31.7 mmol g_{cat}^{-1} h^{-1}) fourfold, achieving high selectivity (above 90%) and excellent regeneration capability in selective methane oxidation under mild conditions at 80 °C compared to non-activated BNC catalysts. Spectroscopic and microscopic techniques confirmed that oxygen-incorporated BO_x species predominantly form on disordered boron sites of BNC, particularly at the edges and surfaces of BN particles. Mechanistic studies, combining experimental and theoretical approaches, demonstrated that both H_2O and O_2 are essential for activation, proceeding via a radical-driven pathway. This work presents an effective activation strategy for non-metallic BN under mild and clean conditions, highlighting its significant potential for low-temperature selective oxidation of important alkanes.

CRediT authorship contribution statement

Younhwa Kim: Conceptualization, Formal analysis, Validation, Investigation, Methodology, Software, Funding acquisition, Writing – original draft. Hobin Kwak: Formal anlaysis, Investigation (performed additional experiments on reaction tests, EPR, and UV–vis analyses). Chanhee Choi: Formal anlaysis, Investigation Investigation (performed additional experiments on NMR, SEM and TEM analyses). Hyesung Choi: Formal analysis, Investigation (performed NEXAFS experiments). Sungsu Kang: Formal analysis, Investigation (performed TEM experiments). Chan Kim: Formal analysis, Investigation (performed additional experiments on in situ DRIFTS analysis). Yongmin Kim: Investigation (in situ DRIFTS analysis). Jungwon Park: Supervision, Conceptualization, Funding acquisition, Investigation, Writing – review and editing.

Declaration of competing interest

The authors declare that they have no known competing financial interests or personal relationships that could have appeared to influence the work reported in this paper.

Acknowledgments

This work was supported by Basic Science Research Program through the National Research Foundation of Korea (NRF) funded by the Ministry of Education (2021R1A6A3A01087254). This work was also supported by the Institute for Basic Science (Grant No. IBS-R006-D1) and the NRF Grant funded by the Korean government (RS-2024-00421181 and RS-2024-00449965).

Appendix A. Supplementary data

Supplementary data to this article can be found online at https://doi.org/10.1016/j.cej.2025.165419.

Data availability

Data will be made available on request.

References

[1] H. Chen, D.-e. Jiang, Z. Yang, S. Dai, Engineering nanostructured interfaces of hexagonal boron nitride-based materials for enhanced catalysis, Acc. Chem. Res. 56 (2022) 52–65.
[2] J.T. Grant, C.A. Carrero, F. Goeltl, J. Venegas, P. Mueller, S.P. Burt, S. Specht, W. McDermott, A. Chieregato, I. Hermans, Selective oxidative dehydrogenation of propane to propene using boron nitride catalysts, Science 354 (2016) 1570–1573.
[3] L. Shi, Y. Wang, B. Yan, W. Song, D. Shao, A.-H. Lu, Progress in selective oxidative dehydrogenation of light alkanes to olefins promoted by boron nitride catalysts, Chem. Commun. 54 (2018) 10936–10946.
[4] M. Ravi, M. Ranocchiari, J.A. van Bokhoven, The direct catalytic oxidation of methane to methanol—a critical assessment, Angew. Chem. Int. Ed. 56 (2017) 16464–16483.

[5] Y. Kim, T.Y. Kim, H. Lee, J. Yi, Distinct activation of cu-MOR for direct oxidation of methane to methanol, Chem. Commun. 53 (2017) 4116–4119.
[6] Y. Kim, T.Y. Kim, C.K. Song, K.R. Lee, S. Bae, H. Park, D. Yun, Y.S. Yun, I. Nam, J. Park, Redox-driven restructuring of lithium molybdenum oxide nanoclusters boosts the selective oxidation of methane, Nano Energy 82 (2021) 105704.
[7] X. Tang, L. Wang, B. Yang, C. Fei, T. Yao, W. Liu, Y. Lou, Q. Dai, Y. Cai, X.-M. Cao, Direct oxidation of methane to oxygenates on supported single cu atom catalyst, Appl. Catal. B Environ. 285 (2021) 119827.
[8] N. Yang, Y. Zhao, P. Wu, G. Liu, F. Sun, J. Ma, Z. Jiang, Y. Sun, G. Zeng, Defective C_3N_4 frameworks coordinated diatomic copper catalyst: towards mild oxidation of methane to C1 oxygenates, Appl. Catal. B Environ. 299 (2021) 120682.
[9] P. Han, R. Yan, Y. Wei, L. Li, J. Luo, Y. Pan, B. Wang, J. Lin, S. Wan, H. Xiong, Mechanistic insights into radical-induced selective oxidation of methane over nonmetallic boron nitride catalysts, J. Am. Chem. Soc. 145 (2023) 10564–10575.
[10] L. Yang, H. Lin, Z. Fang, Y. Yang, X. Liu, G. Ouyang, Recent advances on methane partial oxidation toward oxygenates under mild conditions, Renew. Sust. Energ. Rev. 184 (2023) 113561.
[11] Y. Kim, S. Kang, D. Kang, K.R. Lee, C.K. Song, J. Sung, J.S. Kim, H. Lee, J. Park, J. Yi, Single-phase formation of Rh2O3 nanoparticles on h-BN support for highly controlled methane partial oxidation to syngas, Angew. Chem. Int. Ed. 60 (2021) 25411–25418.
[12] M.J. Boyd, A.A. Latimer, C.F. Dickens, A.C. Nielander, C. Hahn, J.K. Nørskov, D. C. Higgins, T.F. Jaramillo, Electro-oxidation of methane on platinum under ambient conditions, ACS Catal. 9 (2019) 7578–7587.
[13] J. Oh, A. Boucly, J.A. van Bokhoven, L. Artiglia, M. Cargnello, Palladium catalysts for methane oxidation: old materials, new challenges, Acc. Chem. Res. 57 (2023) 23–36.
[14] B. Yu, L. Cheng, S. Dai, Y. Jiang, B. Yang, H. Li, Y. Zhao, J. Xu, Y. Zhang, C. Pan, Silver and copper dual single atoms boosting direct oxidation of methane to methanol via synergistic catalysis, Adv. Sci. 10 (2023) 2302143.
[15] B. Yu, L. Cheng, J. Wu, B. Yang, H. Li, J. Xu, Y. Zhang, C. Pan, X.-M. Cao, Y. Zhu, Surface hydroxyl group dominating aerobic oxidation of methane below room temperature, Energ, Environ. Sci. 17 (2024) 8127–8139.
[16] J. Shan, M. Li, L.F. Allard, S. Lee, M. Flytzani-Stephanopoulos, Mild oxidation of methane to methanol or acetic acid on supported isolated rhodium catalysts, Nature 551 (2017) 605–608.
[17] W. Li, Z. Li, H. Zhang, P. Liu, Z. Xie, W. Song, B. Liu, Z. Zhao, Efficient catalysts of surface hydrophobic cu-BTC with coordinatively unsaturated cu (I) sites for the direct oxidation of methane, Proc. Natl. Acad. Sci. 120 (2023) e2206619120.
[18] Z. Jin, L. Wang, E. Zuidema, K. Mondal, M. Zhang, J. Zhang, C. Wang, X. Meng, H. Yang, C. Mesters, Hydrophobic zeolite modification for in situ peroxide formation in methane oxidation to methanol, Science 367 (2020) 193–197.
[19] Y. Kim, H. Choi, T.Y. Kim, S. Kang, C. Choi, J. Kim, C.K. Song, J. Sung, J.W. Han, J. Park, Lattice-disordered boron nitride colloidal catalyst for low-temperature selective methane oxidation, ACS Catal. 14 (2024) 15622–15632.
[20] Y. Kwon, T.Y. Kim, G. Kwon, J. Yi, H. Lee, Selective activation of methane on single-atom catalyst of rhodium dispersed on zirconia for direct conversion, J. Am. Chem. Soc. 139 (2017) 17694–17699.
[21] Y. Xu, D. Wu, P. Deng, J. Li, J. Luo, Q. Chen, W. Huang, C.M. Shim, C. Jia, Z. Liu, Au decorated Pd nanowires for methane oxidation to liquid C1 products, Appl. Catal. B Environ. 308 (2022) 121223.
[22] L. Wu, W. Fan, X. Wang, H. Lin, J. Tao, Y. Liu, J. Deng, L. Jing, H. Dai, Methane oxidation over the zeolites-based catalysts, Catalysts 13 (2023) 604.
[23] M.S. Kim, K.H. Park, S.J. Cho, E.D. Park, Partial oxidation of methane with hydrogen peroxide over Fe-ZSM-5 catalyst, Catal. Today 376 (2021) 113–118.
[24] J.M. Venegas, Z. Zhang, T.O. Agbi, W.P. McDermott, A. Alexandrova, I. Hermans, Why boron nitride is such a selective catalyst for the oxidative dehydrogenation of propane, Angew. Chem. Int. Ed. 59 (2020) 16527–16535.
[25] Z. Liu, B. Yan, S. Meng, R. Liu, W.D. Lu, J. Sheng, Y. Yi, A.H. Lu, Plasma tuning local environment of hexagonal boron nitride for oxidative dehydrogenation of propane, Angew. Chem. Int. Ed. 60 (2021) 19691–19695.
[26] A. Pakdel, Y. Bando, D. Golberg, Plasma-assisted interface engineering of boron nitride nanostructure films, ACS Nano 8 (2014) 10631–10639.
[27] T. Sainsbury, A. Satti, P. May, Z. Wang, I. McGovern, Y.K. Gun'ko, J. Coleman, Oxygen radical functionalization of boron nitride nanosheets, J. Am. Chem. Soc. 134 (2012) 18758–18771.
[28] D. Lee, B. Lee, K.H. Park, H.J. Ryu, S. Jeon, S.H. Hong, Scalable exfoliation process for highly soluble boron nitride nanoplatelets by hydroxide-assisted ball milling, Nano Lett. 15 (2015) 1238–1244.
[29] F. Xiao, S. Naficy, G. Casillas, M.H. Khan, T. Katkus, L. Jiang, H. Liu, H. Li, Z. Huang, Hydrogels: edge-hydroxylated boron nitride Nanosheets as an effective additive to improve the thermal response of hydrogels, Adv. Mater. 27 (2015) 7196–7203.
[30] F. Hayee, L. Yu, J.L. Zhang, C.J. Ciccarino, M. Nguyen, A.F. Marshall, I. Aharonovich, J. Vučković, P. Narang, T.F. Heinz, Revealing multiple classes of stable quantum emitters in hexagonal boron nitride with correlated optical and electron microscopy, Nat. Mater. 19 (2020) 534–539.
[31] A.L. Gibb, N. Alem, J.-H. Chen, K.J. Erickson, J. Ciston, A. Gautam, M. Linck, A. Zettl, Atomic resolution imaging of grain boundary defects in monolayer chemical vapor deposition-grown hexagonal boron nitride, J. Am. Chem. Soc. 135 (2013) 6758–6761.
[32] S. Kang, J. Cha, Y.S. Jo, Y.J. Lee, H. Sohn, Y. Kim, C.K. Song, Y. Kim, D.H. Lim, J. Park, Heteroepitaxial growth of B5-site-rich Ru nanoparticles guided by hexagonal boron nitride for low-temperature Ammonia dehydrogenation, Adv. Mater. 35 (2023) 2203364.
[33] Y. Cao, P. Maitarad, M. Gao, T. Taketsugu, H. Li, T. Yan, L. Shi, D. Zhang, Defect-induced efficient dry reforming of methane over two-dimensional Ni/h-boron nitride nanosheet catalysts, Appl. Catal. B Environ. 238 (2018) 51–60.
[34] Q. Zhang, X. Tang, Y. Zhou, Y. Shi, L. Ni, J. Xu, C. Pan, Y. Zhang, B. Mu, Y. Guo, Establishing metal-nonoxygen bonds to improve thermal stability of Pt_1/CeO_2 via coating boron nitride, Chem. Eng. Sci. 302 (2025) 120856.
[35] D.W. O'Sullivan, M. Tyree, The kinetics of complex formation between Ti (IV) and hydrogen peroxide, Int. J. Chem. Kinet. 39 (2007) 457–461.
[36] Z. Liu, J. Liu, S. Mateti, C. Zhang, Y. Zhang, L. Chen, J. Wang, H. Wang, E. H. Doeven, P.S. Francis, Boron radicals identified as the source of the unexpected catalysis by boron nitride nanosheets, ACS Nano 13 (2019) 1394–1402.
[37] W. Zhu, X. Gao, Q. Li, H. Li, Y. Chao, M. Li, S.M. Mahurin, H. Li, H. Zhu, S. Dai, Controlled gas exfoliation of boron nitride into few-layered nanosheets, Angew. Chem. Int. Ed. 128 (2016) 10924–10928.
[38] J. Liu, Y. Li, C. Jin, H. Lin, H. Li, Effect and mechanism analysis of hydroxylated nano-boron nitride on workability and multi-scale mechanical properties of cement paste, Arch. Civil Mech. Eng. 22 (2022) 122.
[39] P. Chaturbedy, M. Ahamed, M. Eswaramoorthy, Oxidative dehydrogenation of propane over a high surface area boron nitride catalyst: exceptional selectivity for olefins at high conversion, ACS Omega 3 (2018) 369–374.
[40] D.M. Marincel, M. Adnan, J. Ma, E.A. Bengio, M.A. Trafford, O. Kleinerman, D. V. Kosynkin, S.-H. Chu, C. Park, S.J. Hocker, Scalable purification of boron nitride nanotubes via wet thermal etching, Chem. Mater. 31 (2019) 1520–1527.
[41] N. Konoshchuk, O. Rozovik, G. Fedorenko, V. Koshechko, V. Pokhodenko, Functionalized graphene-like boron nitride prepared Mechanochemically and its nanocomposite with folic acid, Theor. Exp. Chem. (2025) 1–12.
[42] J.-M. Li, Robust 2D room-temperature dilute ferrimagnetism enhancement in freestanding ammoniated atom-thin [0001] h-BN nanoplates, ACS Appl. Mater. Interfaces 9 (2017) 39626–39634.
[43] A. Katzir, J. Suss, A. Zunger, A. Halperin, Point defects in hexagonal boron nitride. I. EPR, thermoluminescence, and thermally-stimulated-current measurements, Phys. Rev. B 11 (1975) 2370.
[44] Q. Lu, Q. Zhao, T. Yang, C. Zhai, D. Wang, M. Zhang, Preparation of boron nitride nanoparticles with oxygen doping and a study of their room-temperature ferromagnetism, ACS Appl. Mater. Interfaces 10 (2018) 12947–12953.
[45] M. Fanciulli, T. Moustakas, EPR investigation of defects in boron nitride thin films, MRS Online Proceedings Library (OPL) 242 (1992) 605.
[46] J. MacNaughton, A. Moewes, R. Wilks, X. Zhou, T. Sham, T. Taniguchi, K. Watanabe, C. Chan, W. Zhang, I. Bello, Electronic structure of boron nitride single crystals and films, Phys. Rev. B 72 (2005) 195113.
[47] S. Hong, C.-S. Lee, M.-H. Lee, Y. Lee, K.Y. Ma, G. Kim, S.I. Yoon, K. Ihm, K.-J. Kim, T.J. Shin, Ultralow-dielectric-constant amorphous boron nitride, Nature 582 (2020) 511–514.
[48] A. L'Hermitte, D.M. Dawson, P. Ferrer, K. Roy, G. Held, T. Tian, S.E. Ashbrook, C. Petit, Formation mechanism and porosity development in porous boron nitride, J. Phys. Chem. C 125 (2021) 27429–27439.
[49] E.D. Mistry, D. Lubert-Perquel, I. Nevjestic, G. Mallia, P. Ferrer, K. Roy, G. Held, T. Tian, N.M. Harrison, S. Heutz, Paramagnetic states in oxygen-doped boron nitride extend light harvesting and photochemistry to the deep visible region, Chem. Mater. 35 (2023) 1858–1867.
[50] Q. Weng, D.G. Kvashnin, X. Wang, O. Cretu, Y. Yang, M. Zhou, C. Zhang, D. M. Tang, P.B. Sorokin, Y. Bando, Tuning of the optical, electronic, and magnetic properties of boron nitride nanosheets with oxygen doping and functionalization, Adv. Mater. 29 (2017) 1700695.
[51] V.L. Sushkevich, D. Palagin, M. Ranocchiari, J.A. Van Bokhoven, Selective anaerobic oxidation of methane enables direct synthesis of methanol, Science 356 (2017) 523–527.
[52] C.C. Zhang, X. Gao, B. Yilmaz, Development of FTIR spectroscopy methodology for characterization of boron species in FCC catalysts, Catalysts 10 (2020) 1327.
[53] Z. Wu, K. Wang, W. Sun, Z. Li, Z. Ma, Y. Zhu, Y. Zou, Y. Zhang, Defective boron nitride inducing the Lithium-ion migration on the sub-surface of $LiBH_4$, Adv. Funct. Mater. 32 (2022) 2205677.
[54] X. Sun, X. Chen, C. Fu, Q. Yu, X.-S. Zheng, F. Fang, Y. Liu, J. Zhu, W. Zhang, W. Huang, Molecular oxygen enhances H_2O_2 utilization for the photocatalytic conversion of methane to liquid-phase oxygenates, Nat. Commun. 13 (2022) 6677.
[55] H. Zhou, F. Chen, D. Liu, X. Qin, Y. Jing, C. Zhong, R. Shi, Y. Liu, J. Zhang, Y. Zhu, Boosting reactive oxygen species formation over Pd and VO_8 co-modified TiO_2 for methane oxidation into valuable oxygenates, Small 20 (2024) 2311355.
[56] J. Liu, Y. Wei, R. Li, Y. Liu, H. Yu, X. Zhou, B. Wu, T. Lin, L. Zhong, Isolated Ni sites anchored on zeolites for direct synthesis of acetic acid from methane oxidative carbonylation, Appl. Catal. B: Environ. Energy 350 (2024) 123951.